Large eddy simulations of oxy-fuel combustors for direct-fired supercritical CO_2 power cycles

Daniel T. Banuti[1]
Cascade Technologies, Inc.
Palo Alto, CA

Lee Shunn[2]
Cascade Technologies, Inc.
Palo Alto, CA

Sanjeeb Bose
Cascade Technologies, Inc.
Palo Alto, CA

Dokyun Kim
Cascade Technologies, Inc.
Palo Alto, CA

ABSTRACT

Supercritical direct-fired CO_2 cycles promise higher efficiencies with a smaller build, while achieving a complete capture of combustion products for a future generation of carbon-neutral power plants. However, practical component design is still in its infancy, complicated by the extreme conditions with combustion chamber pressures in excess of 20 MPa, and CO_2 injection temperatures of the order of 1000 K. In the present paper we perform large eddy simulations of different injector configurations of such a combustor. We compare swirl injection based on gas turbines with coaxial injection based on rocket engines, using different strategies to add bypass CO_2. An analysis of the local thermodynamic states shows that, unexpectedly, highly CO_2-diluted high-pressure combustion of methane with oxygen shows moderate real fluid effects even in the flame zone. Furthermore, the critical strain rate is very sensitive to the chemical mechanism, thus invoking uncertainties in injector design.

INTRODUCTION

In the pursuit of ensuring power supply while reducing CO_2 emissions, cycles using supercritical CO_2 (sCO2) as working fluids promise higher efficiencies at significantly smaller builds [1]. The Allam cycle in particular is a new concept that additionally allows for a complete capture of the combustion products at sequestration-ready pressures [14]. Heat addition occurs in direct-fired oxy-fuel sCO2 combustors, where fuel (e.g. natural gas) and oxygen are injected and burnt directly in the sCO2 stream, without requiring an additional heat exchanger. In this way, formation of nitrous oxides is avoided altogether, CO_2 can be tapped off the cycle at high pressures commercial applications or sequestration [9]. While thermodynamic cycle analysis [14] provides required global mass flow rates, the practical design and implementation into a technical system is still in its infancy. Particularly the combustor design is still an area of active research: suggested concepts include jets in crossflow [14], trapped vortex mixing chambers [13], gas turbine-like combustion chambers with swirl injectors [13], and coaxial injectors in a rocket preburner-like geometry [29, 12].

However, multi-scale interactions between turbulence and chemistry remain an unresolved issue in theoretical, experimental, and numerical investigations of high-pressure complex environments. CFD can play an important role in optimizing cycle efficiency in supercritical systems. The characteristic operating conditions of direct-fired sCO2 cycles involve turbine inlet temperatures and pressures of order 1100-1400 K and 250-300 bars, respectively [1]; thermodynamic conditions in the combustor may be predominantly supercritical, the fluid mixture in principle departs from ideal-gas behavior.

Simulation and analysis is impeded by the fluid properties at the projected combustor conditions. Data concerning chemical kinetics and transport properties in high-pressure, CO_2 diluted flow is lacking substantially [19], real fluid effects are often expected for injection at supercritical pressures. Operated at comparable pressures, injection in rocket engine combustion has been studied thoroughly [24, 23, 10]: The injected fluid undergoes a

---

heating process as it adapts to chamber conditions; the molecular structure changes from liquid to gaseous [8, 4, 3]. At subcritical pressures, this process intersects the coexistence line; ligaments and droplets are formed, separated from the vapor phase by a sharp interface. Beyond the critical point, the injection process is smooth, sharp interfaces are replaced by a diffuse mixing layer [10, 20].

So far, different injector concepts have not been directly compared in the literature, nor have the effects of real fluid effects been assessed on direct-fires sCO2 combustor flows. In the present paper, we seek to remedy this using large eddy simulations and 1D counterflow flame solutions. We will discuss progress and results in application of the in-house CFD code CharLES, to accurately represent oxy-fuel combustors for direct-fired supercritical CO2 power cycles. CharLES is a massively-parallel, high-fidelity multiphysics CFD solver that has been successfully applied to a number of related flow problems, including atomization (Li et al. [17]), combustion in gas turbines (Mueller and Pitsch [22]) and high-speed flow (Saghafian et al. [27]). We will discuss unsteady flow fields that cannot be obtained using RANS simulations.

METHODS

Large eddy simulations were carried out using the CharLES solver, an in-house development of Cascade Technologies. CharLES is a high order, finite volume, compressible flow solver which has successfully been applied to other compressible combustion cases [27]. An in-house entropy-stable flux scheme motivated by Tadmor [30] ensures low dissipation. Sub-grid-scale closure is reached using Vreman's model [31].

Combustion is modeled using a flamelet progress variable approach [25], the concept is illustrated in Fig. 1. Steady diffusion flamelets were solved over a range of strain rates and presented as a function of the fuel mixture fraction Z. In non-premixed combustion, the instantaneous strain rate is conveniently characterized by the scalar dissipation rate

$$\chi = 2D|\nabla Z|^2, \tag{1}$$

where D is the mass diffusivity. χ has units of s^{-1} and can be interpreted as an inverse diffusion timescale.
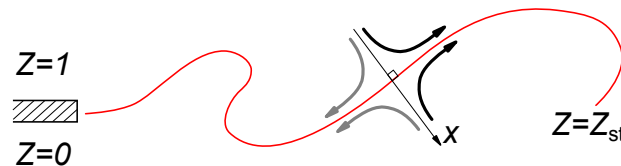

Figure 1: Flamelet models assume that the turbulent flame front between oxidizer ($Z = 0$) and fuel ($Z = 1$) can be understood as being locally composed of elementary flamelets. These flamelets are formed as 1D counterflow diffusion flames, their structure varies with the strain rate. The ensemble of possible flamelets is stored in a table, during runtime local fluid properties are determined through look-up.

GRI-Mech 3.0 is a widely-used mechanism for natural gas combustion containing 53 species and 325 reactions [28]. Rate parameters have been optimized against measurements of ignition delay time, species profiles, laminar flame speed, flow reactors, and NO formation. Although some of the training data includes experiments up to 84 atm, the vast majority of optimization targets are from atmospheric reactors.

AramcoMech 1.3 is a detailed kinetic mechanism that describes a large number of C1-C4 based hydrocarbon and oxygenated fuels [21]. It consists of 253 species and 1542 reactions and has been validated against experimental data from shock tubes, rapid compression machines, flames, and flow reactors. A unique aspect of AramcoMech is that it includes pressure-dependent reaction rates that (in some cases) have been optimized against target data up to 260 atm. Not all of the reactions have experimental support at these high pressures; however, pressure fits are included for 79 reactions and cover pressures up to at least 100 atm in 43 reactions.

In this study, ideal gas behavior is assumed for all components based on the high temperatures. However, a review of this assumption based on thermodynamic trajectories [5, 6] will be performed.

A BRIEF REVIEW OF HIGH PRESSURE THERMODYNAMICS

The pressure–temperature state space

Direct-fired supercritical CO_2 combustors are characterized by the supercritical thermodynamic conditions under which they operate. However, it has become clear that 'supercritical', i.e. at temperatures and pressures exceeding the fluid critical temperatures T_{cr} and pressures p_{cr}, does not yield sufficient information to uniquely determine fluid properties. To quantify real fluid effects, we use the classical compressibility factor $\mathcal{Z}$ [2], defined as

$$\mathcal{Z} = \frac{p}{\rho R T}, \tag{2}$$

which can be interpreted as the nondimensional ratio of the pressure p in the fluid, compared to the pressure an ideal gas with the respective density ρ and temperature T would exert. Then, ideal gas behavior can be expected for $\mathcal{Z} = 1$, real gas behavior otherwise. Following the corresponding states principle [2], thermodynamic state variables are most general in their reduced form, nondimensionalized with the respective critical parameter, yielding the reduced pressure $p_r = p/p_{cr}$ and reduced temperature $T_r = T/T_{cr}$.
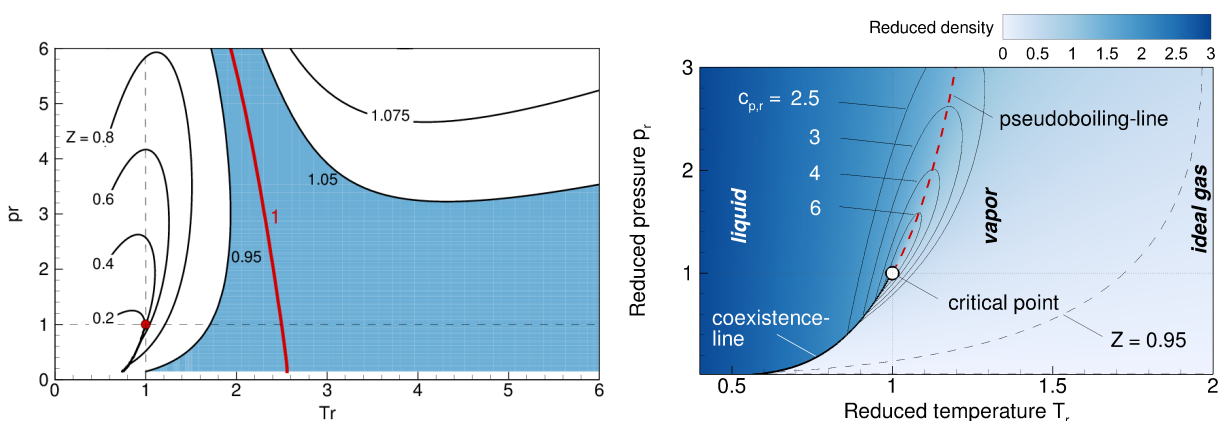

Figure 2: Compressibility $\mathcal{Z}$ in reduced temperature T_r and pressure p_r diagram. Supercritical fluids may behave like ideal gases, subcritical gases may exhibit significant real fluid effects. (left) shaded region with 5% deviation to ideal gas behavior; (right) close-up of near-critical region shows transition from supercritical liquid to gaseous behavior across the pseudoboiling line, accompanied by heat capacities that exceed the respective liquid and gaseous values significantly. From Banuti et al. [7, 8].

Figure 2 shows how real fluid effects are distributed in the state space, revealing that there is no physical justification to differentiate fluid properties using the quadrants formed by the critical isobar and isotherm, respectively. Instead, it seems more illustrative to realize that low temperature liquid states transform to gaseous states across the coexistence line and its supercritical extension, the 'pseudoboiling' or 'Widom' line [3, 7]. Ideal gas states are approached for $T_r > 2$, but strictly only reached along a line. When pressures exceed $p_r > 3$, real fluid effects become more pronounced.

The mixture state

While Figure 2 is readily constructed from tabulated pure fluid data, the reduced parameters of a combustion chamber depend on the mixture properties, and thus changes locally. We can conclude that in order to assess the thermodynamic behavior of a sCO2 combustor, we would have to compare its operating condition not merely to the respective critical pressures and temperatures, but to compressibility in the local mixture

A method to analyze the thermodynamic behavior of a flame has been introduced by Banuti et al. [6, 5]. By considering the different mixture states with locally changing composition encountered in a flame, a local reduced temperature $T_r = T/T_{cr}$ and pressure $p_r = p/p_{cr}$ can be determined. The critical properties of the major species are taken from the NIST database [18], the critical properties of the intermediate species can be determined based

3

on their Lennard-Jones potentials [2] and their acentric factor is set to zero, following Giovangigli et al. [15]. The critical properties for the species considered in this study are compiled in Table 1.

While the mixture critical temperature lies between the component pure fluid values, the mixture critical pressure may significantly exceed the pure fluid values. Both are determined using the pseudocritical method described by Reid et al. [26], with

$$T_{\mathrm{mix,cr}} = \sum_{\alpha=1}^{N_S} X_\alpha T_{\alpha,\mathrm{cr}}, \tag{3a}$$

$$p_{\mathrm{mix,cr}} = RT_{\mathrm{mix,cr}} \frac{\sum_{\alpha=1}^{N_S} X_\alpha \mathscr{Z}_{\alpha,\mathrm{cr}}}{\sum_{\alpha=1}^{N_S} X_\alpha v_{\alpha,\mathrm{cr}}}. \tag{3b}$$

Parameters	CH_4	O_2	H_2O	CO_2	CO
T_{cr} [K]	190.6	154.58	647.10	304.2	132.9
p_{cr} [MPa]	4.604	5.043	22.064	7.382	3.499
$\mathscr{Z}_{\mathrm{cr}}$ [-]	0.288	0.288	0.233	0.274	0.295
v_{cr} [cm^3/mol]	98.62	73.37	55.95	94.12	92.165

Table 1: Critical properties of species in H_2/O_2 combustion, where T_{cr}, p_{cr}, v_{cr}, and ω represent, respectively, the critical temperature, critical pressure, critical molar volume and acentric factor of the species.

Then, for each point in the flow field, the respective reduced thermodynamic state can be calculated and compared to a compressibility chart like Fig. 2.

RESULTS

High-pressure chemical kinetics

Chemical kinetic mechanisms for combustion are largely unknown at pressures that are relevant to sCO$_2$ power systems. Even with well-established chemical mechanisms and relatively simple fuels like methane, disparities between mechanisms increase dramatically at high pressures for basic combustion metrics such as flame speed and ignition delay time [16]. In this section, we compare predictions for characteristic reaction and strain rates using two detailed chemical mechanisms.

In the present example, all 1D flames are simulated at a pressure of 25 MPa, with the reactant compositions and temperatures ($P = 25$ MPa, $X_{\mathrm{O2}}^0 = 0.15, X_{\mathrm{CO2}}^0 = 0.85, T_0 = 1000$ K, $X_{\mathrm{CH4}}^1 = 1.0, T_1 = 300$ K). The calculations assume ideal gas properties. The temperature distributions for different values of the progress variable are shown in Figure 3. Both mechanisms converge to essentially the same temperatures. Similarly, Figs. 4 and 5 show that the attained species distributions are practically indistinguishable. This indicates that the thermodynamic descriptions are consistent between the two mechanisms.

More interestingly, large differences develop for higher scalar dissipation rates. Laminar flame solutions proceed along the burning branch of the S-shaped flame-response curve, moving from near-equilibrium solutions at the upper left towards the extinction point on the right (see Figure 6). An arclength continuation method is used to numerically solve for the pseudo-steady flame solutions on the unstable branch of the S-curve from the extinction point down to the mixing/non-reacting branch. At the extinction strain rate, large scalar gradients drive cold reactants to rapidly diffuse into the inner reactive layer of the flame and dilute the hot products. The resulting cooling overwhelms the Arrhenius reaction rates and the flame extinguishes. The lower branch then represents adiabatic mixing of the unreacted mixture. Consequently, the collection of laminar flame solutions in the S-curve provides insights into how the chemistry (as described by a specific kinetic mechanism) would interact with the strained mixing fields in a turbulent flow. In fact, the extinction point for GRI-Mech 3.0 occurs at a scalar dissipation rate that is approximately 4 times larger than AramcoMech 1.3. AramcoMech also displays more nuanced chemistry in the low- and intermediate-temperature range, as evidenced by the doubly-lobed shape of the curve.

GRI-Mech's resilience to quenching at high strain rates is a result of faster (likely inflated) reaction rates at the target pressure of 25 MPa. Figure 7 compares the overall reaction rate for water predicted by each kinetic
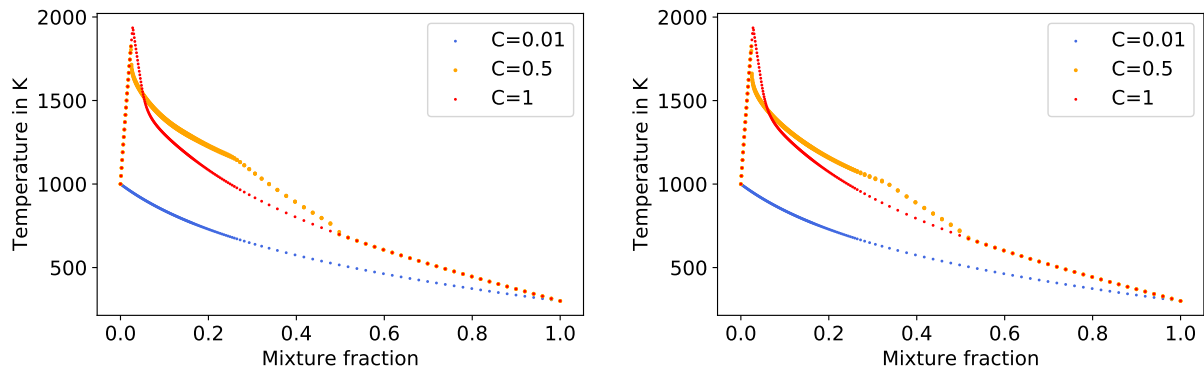
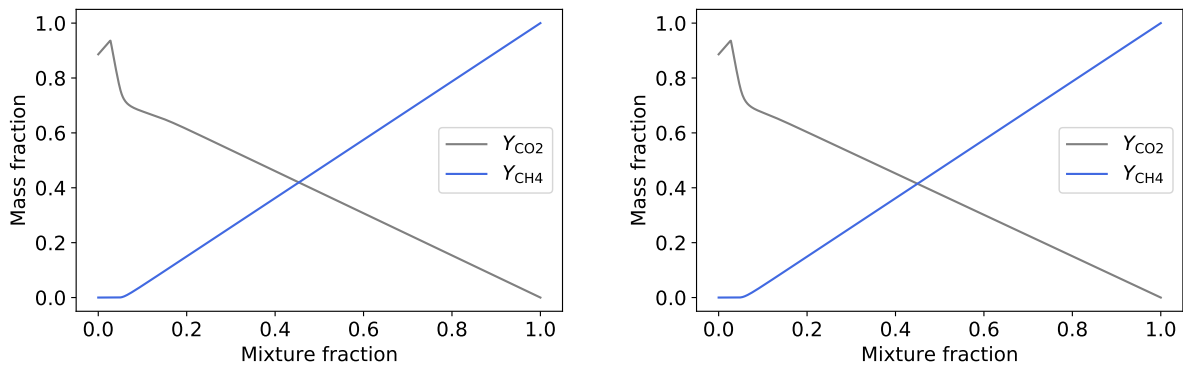Figure 3: Flame temperature. (left) GRI 3.0; (right) Aramco 1.3.

Figure 4: Major species distributions. (left) GRI 3.0; (right) Aramco 1.3.
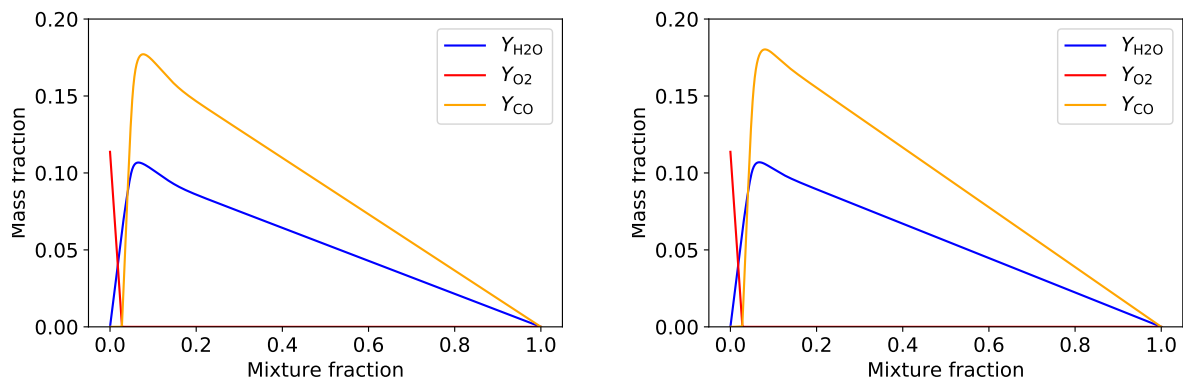

Figure 5: Minor species distributions. (left) GRI 3.0; (right) Aramco 1.3.

mechanism. Although the burned mass fraction for this representative product species is the same for both mechanisms, the reaction rates are much faster in GRI-Mech 3.0 than AramcoMech 1.3. Since rate parameters in GRI-Mech are fit largely from low-pressure data, production rates are likely not exhibiting the correct behavior in this high-pressure regime. Moreover, the general balance between reaction timescales and strain-induced
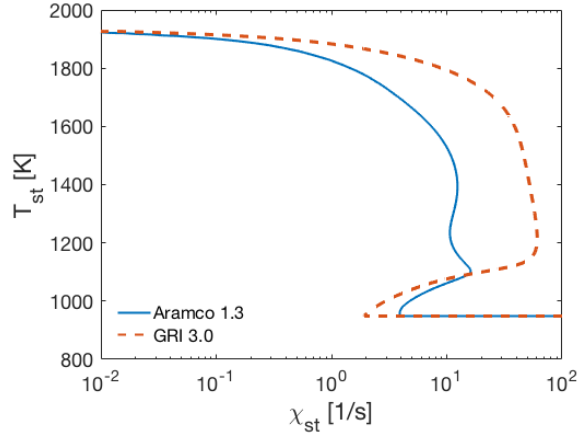
Figure 6: S-curve (flame-response versus scalar dissipation rate) at the stoichiometric condition from laminar diffusion flames using two kinetic mechanisms. GRI-Mech 3.0 is derived largely from low-pressure data, while AramcoMech 1.3 includes some pressure-dependent data.

quenching is an important concept in many turbulent combustion models. In this light, sensitivities such as shown in Figure 6 are alarming and suggest that better high-pressure validation data are needed.
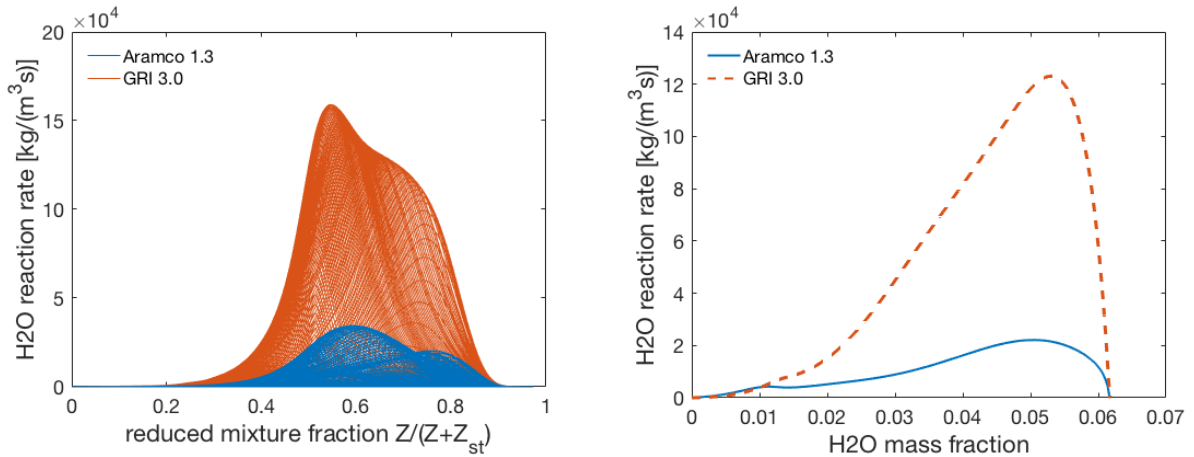

Figure 7: Overall reaction rate for water using two different kinetic mechanisms. (a) Reaction rate versus mixture fraction and (b) reaction rate versus water mass fraction at the stoichiometric mixture.

Thermodynamic flame trajectory

Now that the distributions of temperature and composition across the flames have been calculated, the thermodynamic state in the flame can be assessed using the mixing rules Eqs. (3a),(3b), as introduced in [6, 5]. Figure 8 shows the result. The inflow density of methane deviates about 15% and 20% from ideal gas conditions. Furthermore, it appears that even the flame with its high reduced temperatures comes very close to the $\mathcal{Z} = 1.05$ delimiter. Unfortunately, NIST data for methane is not available for higher temperatures. Strictly, the ideal gas assumption is violated in the fuel stream, and potentially even in the flame, due to the very high pressures. In the present paper, the effect on the flow field will not be studied. It shall be noted however, that the effects are expected to be mitigated, when the correct mass flow rate is used: the underpredicted inflow density will be compensated by an increase in injection velocity in order to achieve the mass flow rate – thus keeping the inflow
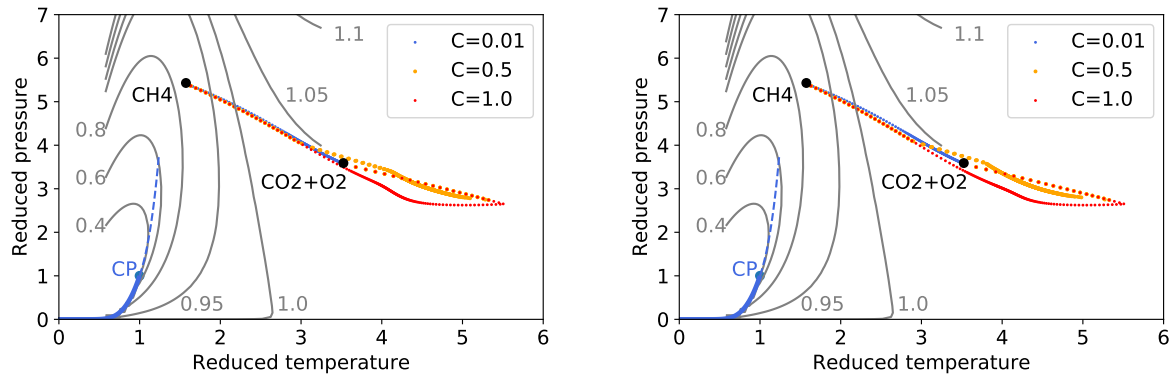
Figure 8: Thermodynamic flame trajectory. (left) GRI 3.0; (right) Aramco 1.3. Blue solid and dashed lines are the coexistence and the Widom line, respectively, separated by the critical point (CP). Gray contour lines correspond to methane compressibility, estimated form NIST [18]. The colored dots represent the local reduced state for each composition in the flame, connecting the reactant states of the oxidizer and fuel streams, marked with black circles.

momentum constant, a prime parameter that determines break-up lengths in injection studies [11].

Large eddy simulation results

sCO$_2$ swirl injector

Figure 9 shows the combustor concept of Delimont et al. [13], serving as a baseline design for a pilot-plant to be realized by the Southwest Research Institute. The concept is comparable to gas turbine combustors: A swirl injector is used to introduce fuel and oxidizer in a liner, where combustion takes place. The liner is embedded into a case that provides additional cooling and dilution flow to control the combustion process and to limit the liner temperature. Here, CO_2 and O_2 form a diluted oxidizer stream in the liner, which is brought into the chamber to be mixed with CH_4. Part of the CO_2 bypasses the injector to be used for dilution and effusion cooling of the chamber liner downstream of the primary reaction zone. Mass flow rates are given in Table 2.
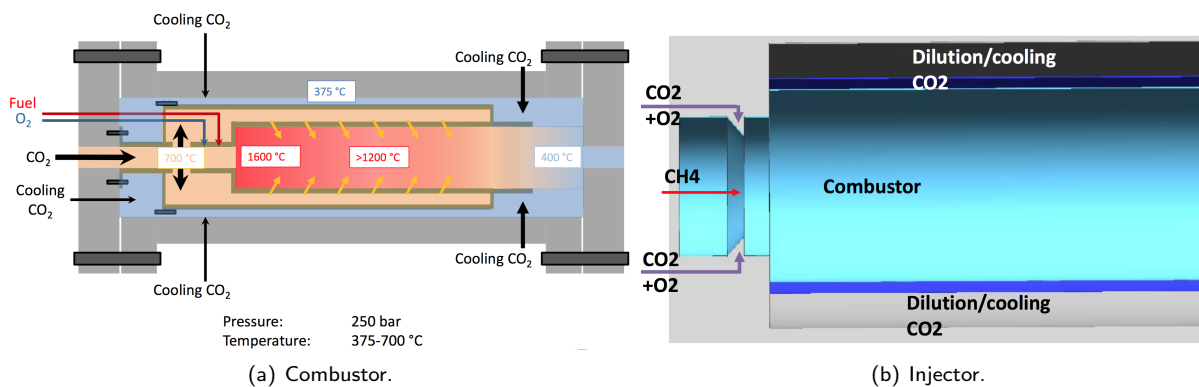

(a) Combustor.

(b) Injector.

Figure 9: Combustor concept from Delimont et al. [13].

Figure 10 shows the geometry and an instantaneous temperature distribution plot. The inflow conditions are given in Table 3, the injection densities ρ_{in} are determined from the NIST database [18], oxygen and carbon dioxide are assumed to mix under ideal gas conditions at their elevated temperature. Injector walls are considered slip walls, the outflow is modeled using a pressure outflow boundary condition with $p = 25$ MPa. Simulations so far have concentrated on the flow inside the liner [13], assuming an effusion type cooling flow. Here we treat

Component	Mass flow in kg/s
CH_4	0.02
O_2	0.08
CO_2 combustor	0.626
CO_2 bypass	0.899
Total	1.625

Table 2: sCO_2 combustor conditions from Delimont et al. [13].

Component	$\dot{m}$ in kg/s	T_{in} in K	ρ_{in} in kg/m^3	X_i	Position
CH_4	0.02	300	186.3	1.0	center
O_2	0.08	1000	90.23	0.15	annulus
CO_2	0.626	1000	125.0	0.85	annulus

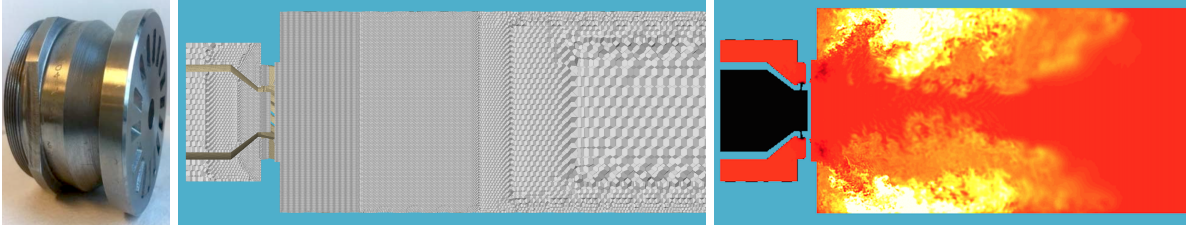Table 3: Injection conditions for sCO_2 combustor simulation.

Figure 10: Swirl injector configuration. (left) photograph of the DLN1 swirl injector, from [13]; (center) mesh in the near-injector region; (right) instantaneous temperature distribution.

the CO_2 bypass flow as a constant mass flux inflow boundary condition distributed equally across faceplate and chamber wall.

The peak temperatures reach 1900 K. The flame is stabilized by the large recirculation zone forming in the wake of the swirl injector. The flame is very sensitive to strain, c.f. Fig. 6, and reaches its maximum temperature away from the injector as the flow impinges onto the wall.

sCO_2 coaxial injector

As an alternative to the swirl injector, we designed a coaxial injector similar to what is found in liquid propellent rocket engines for the same flow rates and chamber diameter specified by Delimont et al. [13]. The goal was to develop an injector that reduces wall heat loads. Figure 11 shows the schematic of a generic coaxial rocket injector. As a baseline, we used a flush injector without recess or taper. The annulus lip is rather thick to facilitate a recirculation zone that helps to attach the flame to the injector, thus increasing combustion stability. Table 4 provides the dimensions. D refers to the chamber diameter, which is set to 2" (0.0508 m), as specified by Delimont et al. [13].

D_0	D_2	D_3	α	L_R	D
0.003	0.005	0.007	0	0	0.0508

Table 4: Geometry of sCO_2 coaxial injector, dimensions in m.

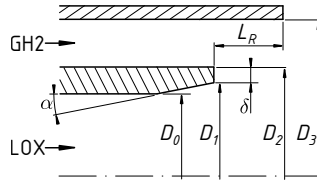The geometry is chosen in order to achieve injection conditions comparable to rocket injectors, Table 3 provides

Figure 11: Generic coaxial injector geometry as used in rocket engines. In the present study, recess L_R and taper α are zero, i.e. inner and outer tube are flush and straight.

the injection boundary conditions. The temperatures are estimated from Delimont et al. [13].

Figure 12 shows the unstructured mesh generated for the case. We use characteristic boundary conditions for the injection of the fuel and oxidizer streams. The mesh is refined in the vicinity of the injector where small scales initiate the shear layer instability. A coarse grid connects the near-injector region to the outflow in order to increase the distance and minimize boundary condition effects on the flame structure, resulting in a final mesh of 5 million control volumes.
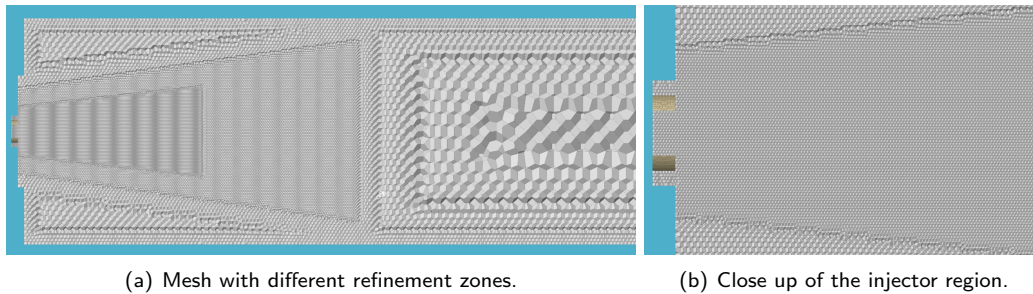

(a) Mesh with different refinement zones.   (b) Close up of the injector region.

Figure 12: Mesh of the coaxial injector sCO$_2$ combustor.

Consistent with rocket injectors, the higher density fluid (here methane) is injected in the center, the lighter oxidizer in the annulus. The respective mole fractions in the annulus are $X_{O2} = 0.15$ and $X_{CO2} = 0.85$, whereas methane is injected pure. The exact injection conditions are given in Table 3.

Figure 13 shows the effect of the annulus flow rate on the flame stabilization and mixing efficiency. Without co-flow, methane is injected into a low velocity background flow induced by the effusion cooling mass flow, Fig. 13(left). Relative velocities are low, the flame is anchored to the injector and remains in a transitional state with insufficient turbulence to ensure efficient mixing. Figure 13(center) shows the case with a co-flow of 0.031 kg/s, in which better mixing is achieved. The flame lifts off, but is stably anchored in a recirculation zone behind the solid central part of the faceplate. Finally, Figure 13(right) shows the nominal mass flow through the annulus, resulting in a well mixed jet with a collapsed methane potential core. Unfortunately, the flame does not remain anchored at the high strain rates and is blown off.

Figure 14 shows the blow-out transient for the high strain rate case. Neither the recirculation behind the solid center faceplate, nor behind the collapsed methane jet suffice to stabilize the flame.

CONCLUSION

We discussed simulations and thermodynamic state analysis of a prototype combustor for direct-fired supercritical CO$_2$ power cycles. These Allam cycles are an exciting new concept that allow for higher cycle efficiency, smaller build, and complete capture of combustion products at sequestration-ready pressures.

Combustor design is in its infancy. We showed temperature fields of a reference swirl injector, related to a projected test facility currently being build by the Southwest Research Institute. The simulation demonstrates how the flame reaches its highest temperatures upon impinging on the wall. The flame is stably anchored in the recirculation zone of the swirl injector.

Due to its similarity to rocket engine properties, we designed a coaxial injector and performed large eddy simulations with the same mass flow rates and chamber geometry as used for the swirl injector case. The flame
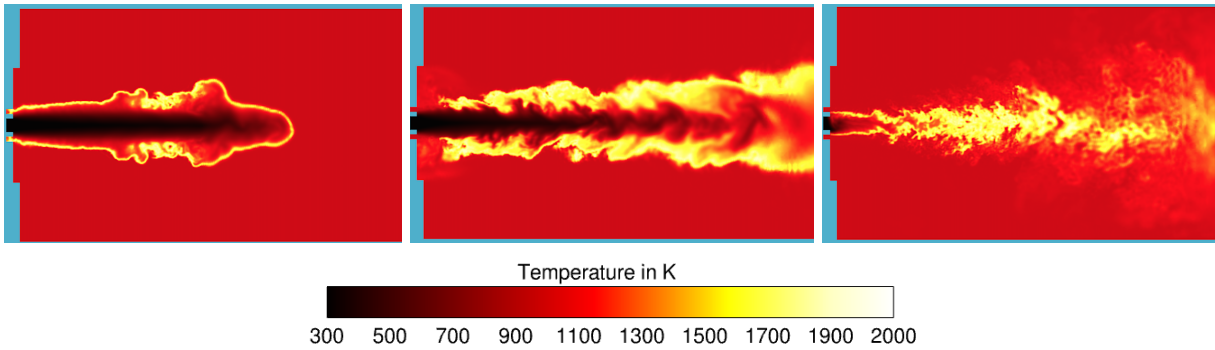
Figure 13: Variation of CO_2/O_2 coflow through the annulus. Mass flow reduced through the annulus is added to the effusion massflow through the outer faceplate. The inner part of the faceplate is an adiabatic wall. (left) no co-flow, all mass flow through faceplate; (center) 0.031 kg/s flow through annulus corresponding to 4.4% nominal, rest added to faceplate; (right) nominal flow through annulus with 0.706 kg/s, unstable.
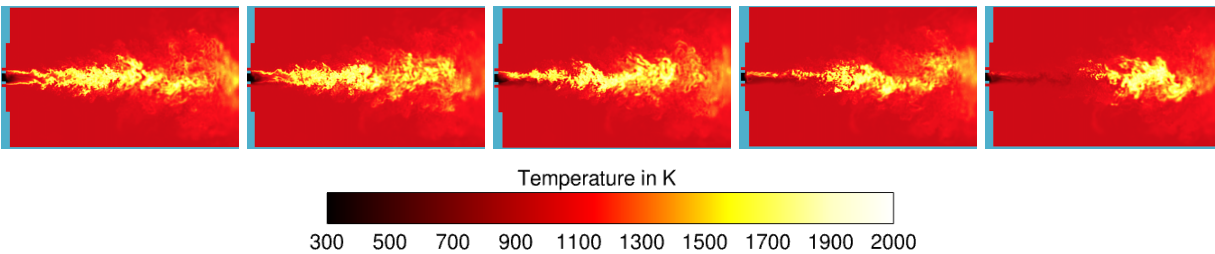

Figure 14: Flame blow-out at high strain rates is captured well with the flamelet progress variable model. Shown are temperature contours for snapshots at different subsequent instances in time, time progresses from left to right.

remains in the center of the chamber, reducing wall temperatures, but is very sensitive to quenching. Stabilization of a lifted flame, however, is possible in a recirculation zone formed by a solid central part of the faceplate.

A comparison of the GRI 3.0 and the Aramco 1.3 chemical mechanisms reveals significant differences in the critical strain rate, imposing uncertainty on the design flow parameters of a coaxial injector that will ensure stable combustion without blow-out.

Unexpectedly, despite the high temperatures, a thermodynamic flame trajectory analysis revealed that for O2-CH4 combustion in CO2 dilution, even the hot reaction zone is exhibiting deviation from ideal gas behavior.

ACKNOWLEDGMENTS

REFERENCES

[1] Y. Ahn, S. J. Bae, M. Kim, S. K. Cho, S. Baik, J. I. Lee, and J. E. Cha. Review of supercritical co2 power cycle technology and current status of research and development. *Nuclear Engineering Technology*, 47:647–661, 2015.

[2] J. M. Prausnitz and R. N. Lichtenthaler and E. Gomes de Azevedo. *Molecular Thermodynamics of Fluid-Phase Equilibria*. Prentice-Hall, 2nd edition edition, 1985.

[3] D. T. Banuti. Crossing the Widom-line – supercritical pseudo-boiling. *Journal of Supercritical Fluids*, 98:12–16, 2015.

[4] D. T. Banuti and K. Hannemann. The absence of a dense potential core in supercritical injection: A thermal break-up mechanism. *Physics of Fluids*, 28(3):035103, 2016.

[5] D. T. Banuti, P. C. Ma, J.-P. Hickey, and M. Ihme. Thermodynamic structure of supercritical LOX-GH2 diffusion flames. *under review*.

[6] D. T. Banuti, P. C. Ma, J.-P. Hickey, and M. Ihme. Sub- or supercritical? a flamelet analysis for high-pressure rocket propellant injection. In *52nd AIAA/SAE/ASEE Joint Propulsion Conference, Propulsion and Energy Forum, AIAA 2016-4789*, Salt Lake City, USA, 2016.

[7] D. T. Banuti, M. Raju, and M. Ihme. Similarity law for widom lines and coexistence lines. *Physical Review E*, 95:052120, May 2017.

[8] D. T. Banuti, M. Raju, P. C. Ma, M. Ihme, and J.-P. Hickey. Seven questions about supercritical fluids towards a new fluid state diagram. In *Proceedings of the 55th AIAA Aerospace Sciences Meeting, AIAA 2017-9144*, Gaylord, USA, 2017.

[9] S.M. Benson and D.R. Cole. Co_2 sequestration in deep sedimentary formations. *Elements*, 4:335–331, 2008.

[10] S. Candel, M. Juniper, G. Singla, P. Scouflaire, and C. Rolon. Structures and dynam- ics of cryogenic flames at supercritical pressure. *Combustion Science and Technology*, 178:161–192, 2006.

[11] B. Chehroudi. Recent experimental efforts on high-pressure supercritical injection for liquid rockets and their implications. *International Journal of Aerospace Engineering*, 2012:121802, 2012.

[12] S. T. Chong, Y. Tang, M. Hassanaly, and V. Raman. Turbulent mixing and combustion of supercritical jets. In *Proceedings of the AIAA Science and Technology Forum and Exposition*, number AIAA 2017-0141, Grapevine, USA, 2017. AIAA.

[13] J. Delimont, N. Andrews, C. Nolen, C. Day, M. Portnoff, L. Chordia, W. Sun, S. Vasu, S. Monahan, and K. McManus. Direct fired oxy-fuel combustor for sco2 power cycles. In *University Turbine Systems Research (UTSR) Project Review Meeting*, Pittsburgh, USA, 2017.

[14] J. Delimont, A. McClung, and M. Portnoff. Simulation of a direct fired oxy-fuel combustor for sCO_2 power cycles. In *The 5th Internationa Symposium - Supercritical CO2 Power Cycles*, San Antonio, USA, 2016.

[15] V. Giovangigli, L. Matuszewski, and F. Dupoirieux. Detailed modeling of planar transcritical H2-O2-N2 flames. *Combustion Theory and Modelling*, 15(2):141–182, 2011.

[16] H. C. Lee, A. A. Mohamad, and L. Y. Jiang. Comprehensive comparison of chemical kinetic mechanisms for syngas/biogas mixtures. *Energy & Fuels*, 29:6126–6145, 2015.

[17] X. Li, M. C. Soteriou, W. Kim, J. M. Cohen, M. Herrmann, F. Ham, D.Kim, H. Le, and J. T. Spyropoulos. High fidelity simulation of the spray generated by a realistic swirling flow injector. In *Proceedings of the ASME Turbo Expo, GT2013-96000*, San Antonio, TX, 2013. ASME.

[18] P. J. Linstrom and W. G. Mallard, editors. *NIST Chemistry WebBook, NIST Standard Reference Database Number 69*, chapter http://webbook.nist.gov. National Institute of Standards and Technology, Gaithersburg MD, 20899, retrieved 2016.

[19] K. R. V. Manikantachari, S. Martin, J. O. Bobren-Diaz, and S. Vasu. Thermal and transport properties for the simulation of direct-fired sco_2 combustor. *Journal of Engineering for Gas Turbines and Power*, 139:121505, 2017.

[20] W. Mayer and H. Tamura. Propellant injection in a liquid oxygen/gaseous hydrogen rocket engine. *Journal of Propulsion and Power*, 12(6):1137–1147, 1996.

[21] W. K. Metcalfe, S. M. Burke, S. S. Ahmed, and H. J. Curran. A hierarchical and comparative kinetic modeling study of C1-C2 hydrocarbon and oxygenated fuels. *Intl. J. Chemical Kinetics*, 45:638–675, 2013.

[22] M. E. Mueller and H. Pitsch. Large eddy simulation of soot evolution in an aircraft combustor. In *Proceedings of the 8th US National Combustion Meeting*, Park City, UT, 2013.

[23] J. C. Oefelein. Thermophysical characteristics of shear-coaxial LOX–H2 flames at supercritical pressure. *Proceedings of the Combustion Institute*, 30(2):2929–2937, 2005.

[24] M. Oschwald, J. J. Smith, R. Branam, J. Hussong, A. Schik, B. Chehroudi, and D. Talley. Injection of fluids into supercritical environments. *Combustion Science and Technology*, 178:49–100, 2006.

[25] C. Pierce and P. Moin. Progress-variable approach for large-eddy simulation of non-premixed turbulent combustion. *Journal of Fluid Mechanics*, 504:73–97, 2008.

[26] R. C. Reid, J. M. Prausnitz, and B. E. Poling. *The properties of gases and liquids*. McGraw Hill, 4th edition, 1987.

[27] A. Saghafian, L. Shunn, D. A. Philips, and F. Ham. Large eddy simulations of the hifire scramjet using a compressible flamelet/progress variable approach. *Proceedings of the Combustion Institute*, 35:2163–2172, 2015.

[28] G. P. Smith, D. M. Golden, M. Frenklach, N. W. Moriarty, B. Eiteneer, M. Goldenberg, C. T. Bowman, R. K. Hanson, S. Song, W. C. Gardiner Jr., V. V. Lissianski, and Z. Qin. GRI-Mech 3.0. http://www.me.berkeley.edu/gri_mech/.

[29] P. Strakey. Oxy-combustion fundamentals for direct-fired cycles. In *University Turbine Systems Research (UTSR) Project Review Meeting*, Pittsburgh, USA, 2017.

[30] E. Tadmor. Entropy stability theory for difference approximations of nonlinear conservation laws and related time-dependent problems. *Acta Numerica*, 12:451–512, 2003.

[31] A. W. Vreman. An eddy-viscosity subgrid-scale model for turbulent shear flow: Algebraic theory and applications. *Physics of Fluids*, 16(10):3670–3681, 2004.